*Sensors and Materials*, Vol. 38, No. 1 (2026) 187–206
MYU Tokyo



S & M 4294

# Spatiotemporal Analysis of Urban Land Surface Temperature and Its Drivers Using Multitemporal Remote Sensing and Spatial Models: Case Study of Chuncheon, South Korea

Zhien Li,[1] Sung-Ho Kil,[2*] Youngkeun Song,[3]
Eunseok Lee,[4] Sang Jin Lee,[5] and Sungmin Lee[6]

[1]Department of Landscape Architecture, Graduate School, Kangwon National University, Gangwon-Dae-Hak-Gil 1, Chuncheon, Gangwondo 24341, Republic of Korea
[2]Department of Ecological Landscape Architecture Design, Kangwon National University, Gangwon-Dae-Hak-Gil 1, Chuncheon, Gangwondo 24341, Republic of Korea
[3]Department of Landscape Architecture, Graduate School of Environmental Studies, Seoul National University, 1 Gwanak-ro, Gwanak-gu, Seoul 08826, Republic of Korea
[4]Architecture & Urban Research Institute, Sejong 30116, Republic of Korea
[5]Institute of Agriculture Science, Chungnam National University, Daejeon 34134, Republic of Korea
[6]Department of Landscape Architecture and Urban Planning, Texas A&M University, College Station, TX, 77843-3137, United States of America

(Received April 17, 2025; accepted November 13, 2025)

***Keywords:*** land surface temperature, ordinary least squares, geographically weighted regression, spatial heterogeneity

Understanding the spatiotemporal dynamics of land surface temperature (*LST*) and its drivers is essential for mitigating urban heat and guiding climate-responsive planning. In this study, we integrate multitemporal remote sensing data derived from satellite sensors with multiresolution image segmentation and spatial regression models to investigate seasonal *LST* patterns and their influencing factors. Seasonal variability is assessed across the year. Analyses are conducted on spatial units consistent across time, and ordinary least squares (OLS) and geographically weighted regression (GWR) models are applied to identify both global and local driving mechanisms. In addition, Getis-Ord Gi* hotspot analysis is employed to delineate core high- and low-temperature zones for focused analysis. Results show pronounced seasonal and spatial heterogeneity. Forest cover and elevation consistently cool *LST*, whereas urban form effects vary by season and location. GWR reveals strong spatial non-stationarity, especially within thermal core zones. The findings highlight the importance of incorporating both spatial heterogeneity and seasonal dynamics in urban heat analysis. The results of this study provide a spatially explicit understanding of *LST* drivers and offer practical insights for climate-adaptive land use and urban design strategies.

*Corresponding author: e-mail: sunghokil@kangwon.ac.kr
https://doi.org/10.18494/SAM5695

ISSN 0914-4935 
https://myukk.org/

## 1. Introduction

With rapid urbanization, the urban thermal environment has become a major concern, as elevated surface temperatures intensify heat stress, increase energy demand, worsen air quality, and degrade ecosystems.[1] A major contributor is the urban heat island (UHI) effect, where impervious surfaces retain heat, making cities significantly warmer than surrounding rural areas.[2,3] Understanding the spatial distribution and drivers of urban thermal patterns is essential for effective mitigation and climate-resilient planning.

Land surface temperature (*LST*) and air temperature (AT) are commonly used to assess urban thermal conditions.[4] While AT reflects human heat stress more directly, its limited spatial coverage restricts its applicability at the urban scale.[5] In contrast, *LST* derived from satellite data offers broad coverage, high resolution, and strong temporal consistency, making it a widely accepted proxy for surface thermal patterns.[6–8] This study utilizes multi-temporal remote sensing data acquired by satellite sensors, particularly the Operational Land Imager (OLI) and Thermal Infrared Sensor (TIRS) aboard Landsat 8. These instruments capture surface-emitted radiation in the TIR spectrum, enabling the accurate retrieval and detailed spatial analysis of *LST*. The accuracy of *LST* largely depends on the TIR data acquired by sensors such as Landsat 8 OLI and TIRS, which detect emitted surface radiation and provide reliable information for retrieving and analyzing the spatial distribution of *LST*. *LST* is influenced by both natural and human factors such as land cover, topography, and urban form.[9–11] Impervious surfaces elevate *LST*, while vegetation and water bodies cool it via evapotranspiration. Elevation is also important, as higher areas tend to be cooler.[12] Urban form significantly influences local ventilation and thermal accumulation. However, the relationship between *LST* and its influencing factors often exhibits spatial non-stationarity, meaning that both the strength and direction of influence vary across locations.[13] Global models like ordinary least squares (OLS) assume uniform effects and may overlook local variation.[14] To address this, we apply a hybrid approach combining OLS and geographically weighted regression (GWR) to capture both global and local effects. Additionally, Getis-Ord Gi* analysis is used to detect *LST* clustering and identify high- and low-temperature core zones.

Although the seasonal variability of *LST* and its drivers have been explored in recent studies, key limitations persist. Many are based on a single time point or season,[12,15] limiting insights into temporal dynamics. Even with multitemporal data, spatial units are often defined by administrative boundaries, which fail to reflect the actual distribution of surface temperature. In this study, we apply multitemporal data and OLS–GWR modeling to examine *LST* patterns, aiming to reveal the mechanisms of urban thermal environments and inform urban planning for climate adaptation.

## 2. Methodology

### 2.1 Study area

This study is focused on Chuncheon (Fig. 1), a city in Gangwon-do, South Korea, with an urbanized area of approximately 333.09 km$^2$. Situated in the northern part of the country, Chuncheon experiences a temperate monsoon climate characterized by distinct seasonal variations. The city's landscape is composed of hills and basins surrounded by mountains, with urban development primarily concentrated in relatively flat lowland areas. This unique combination of topographic and climatic features makes Chuncheon a representative example of a mountainous urban environment in South Korea. It offers a valuable setting for analyzing the spatiotemporal patterns of *LST*, which will provide insights applicable to other mountainous cities with similar climatic conditions.

### 2.2 Data and methods

We integrated Landsat 8 remote sensing imagery with multisource geographic datasets (e.g., land use, elevation, and vegetation indices) to characterize the spatiotemporal patterns of *LST* in the urban area of Chuncheon, South Korea. Regression modeling approaches were subsequently applied to analyze the driving factors influencing *LST* variations. The research methodology encompassed five primary steps (Fig. 2): (1) data preprocessing; (2) the calculation of *LST* and

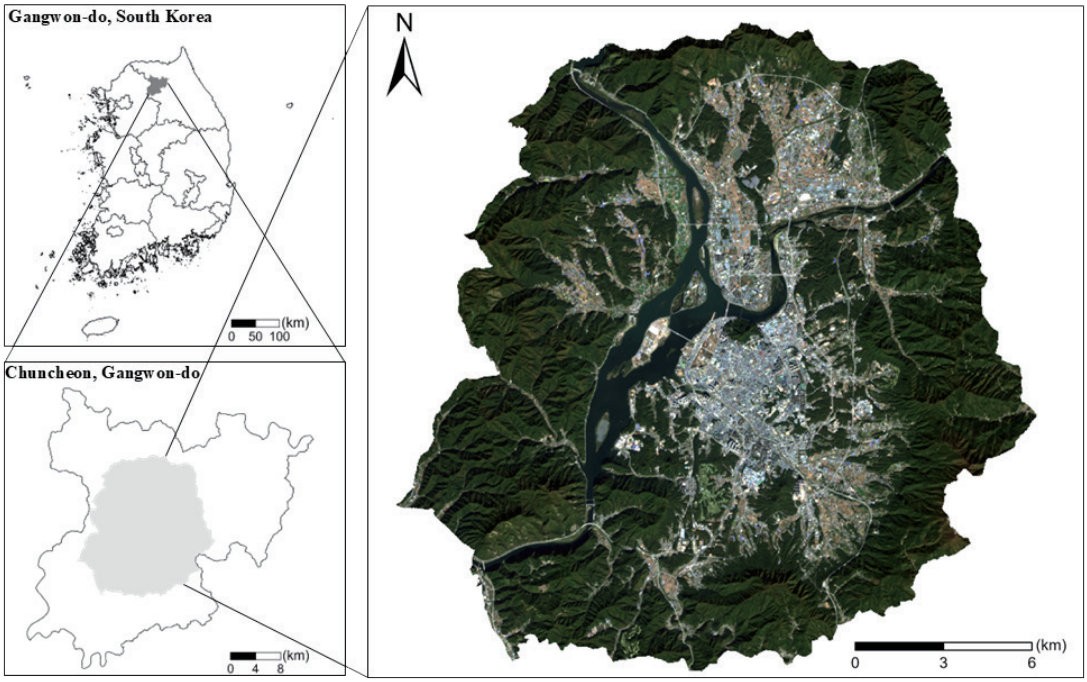


Fig. 1. (Color online) Study area.

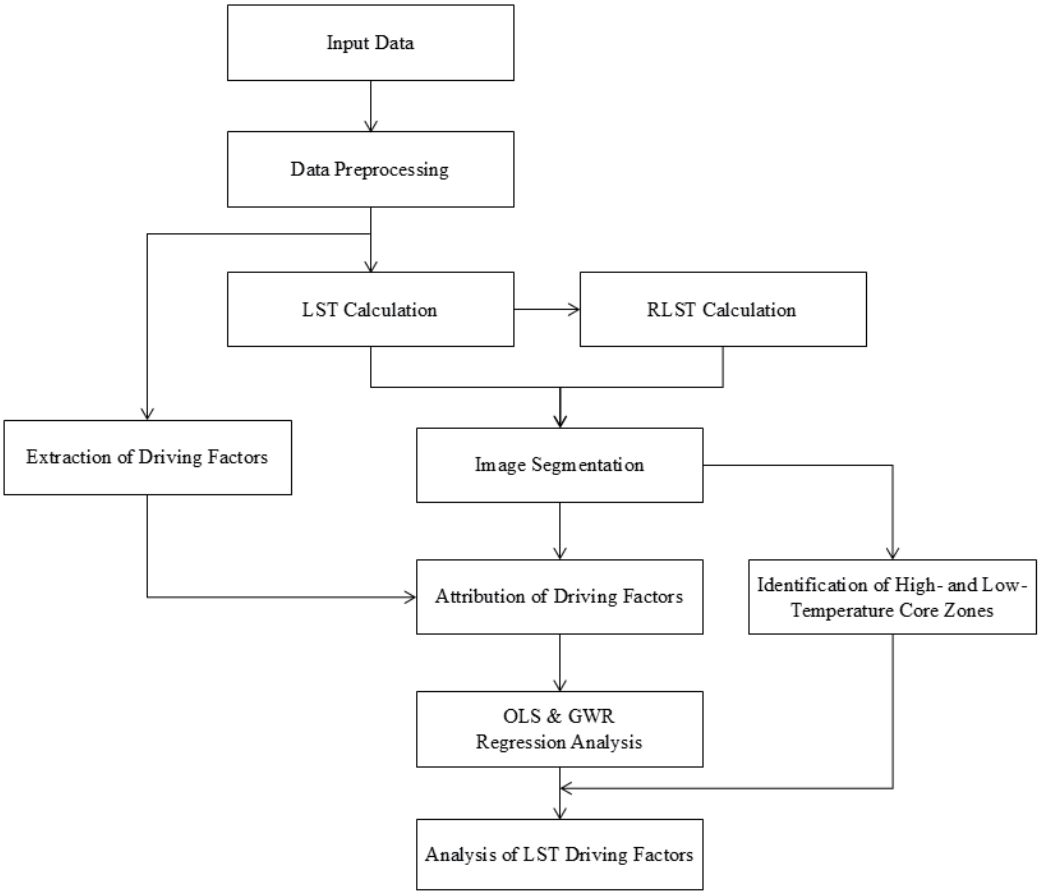


Fig. 2. Research framework.

relative *LST* (*RLST*); (3) the identification of high- and low-temperature core zones; (4) the extraction and assignment of driving factors; and (5) regression analysis using OLS and GWR.

### 2.3 Data description and preprocessing

We utilized multisource geospatial data, including remote sensing imagery, topographic data, land use, and population and urban form data (Table 1). Landsat 8 OLI/TIRS remote sensing imagery provided by the United States Geological Survey (USGS) was employed to calculate *LST* and vegetation indices. Four seasonal Landsat 8 images (March 15, June 19, October 25, and December 28, 2024) were selected to capture the seasonal variations of *LST* in Chuncheon, each with cloud coverage below 10%.

Topographic data were obtained from the Digital Elevation Model (DEM) provided by the Korea Land Information Platform (KLIP), enabling the extraction of elevation and slope data. Land use data consisted of the latest medium-classified land cover dataset (2023), sourced from the Environmental Geographic Information Service (EGIS) of Korea, and were utilized to identify different land use categories. Population and urban form data comprised population

Table 1
Data sources.

| Data type | Data source | Spatial resolution | Temporal resolution |
|---|---|---|---|
| Landsat 8 OLI/TIRS | USGS | 30 m (OLI)<br>100 m (TIRS) | 2024.03.15, 06.19, 10.25, 12.28 |
| DEM | KLIP | 90 m | 2023 |
| Land cover | EGIS | 30 m | 2023 |
| Population data | KLIP | Vector | 2024 |
| Building & road data | V-World | Vector | 2024 |

density from KLIP (2024) and building and road vector datasets from V-World, supporting the analysis of the impacts of urban form and population distribution on thermal conditions.

All data preprocessing was conducted using ArcGIS Pro 3.0 software, standardizing datasets to the WGS 84/UTM Zone 52N coordinate system and resampling them to a consistent spatial resolution of 30 m.

### 2.4 *LST* calculations

Landsat 8 TIRS imagery and the single-channel algorithm[16] were employed to retrieve *LST* for Chuncheon City. Subsequently, *RLST* was calculated to characterize the spatial distribution and temporal variation of surface temperatures across the urban area.

The digital number (DN) of Landsat 8 images was converted to the top of atmosphere (TOA) radiance ($L_\lambda$). The calculation formula is

$$L_\lambda = M_L \times Q_{cal} + A_L - O_i\,, \tag{1}$$

where $M_L$ is the band-specific multiplicative rescaling factor, $Q_{cal}$ represents the DN for Band 10, $A_L$ is the band-specific additive rescaling factor, and $A_L$ is the correction value for Band 10. Both $M_L$ and $A_L$ are radiometric calibration parameters provided in the image metadata.

TOA radiance was then converted into brightness temperature (BT) using

$$BT = \frac{K_2}{\ln\left(\frac{K_1}{L_\lambda} + 1\right)} - 273.15, \tag{2}$$

where $K_1$ and $K_2$ are the thermal conversion constants specific to the sensor. The computed temperature values were converted to degrees Celsius (°C) by subtracting 273.15.

The normalized difference vegetation index (*NDVI*) is an important index to measure the state of vegetation cover and was calculated using (NASA, 2000)

$$NDVI = \frac{NIR - RED}{NIR + RED}, \tag{3}$$

where *NIR* represents the near-infrared band (Band 5) and *RED* represents the red band (Band 4). *NDVI* values range from −1 to +1. High values indicate dense vegetation, while low or negative values typically represent barren surfaces or water bodies.

The proportion of vegetation ($P_v$) was calculated based on *NDVI* using

$$P_v = \left( \frac{NDVI - NDVI_s}{NDVI_v - NDVI_s} \right)^2. \tag{4}$$

According to Ref. 17, *NDVI* values for vegetation and soil are used in the calculation of $P_v$ to apply in global conditions ($NVDI_v = 0.5$ and $NVDI_s = 0.2$).

The estimation of land surface emissivity (LSE, $\varepsilon$) was determined using *NDVI* values:

$$\varepsilon = \varepsilon_v P_v + \varepsilon_s (1 - P_v) + C, \tag{5}$$

where $\varepsilon_v$ and $\varepsilon_s$ represent the emissivity values of vegetation and soil, respectively, and $C$ is the surface roughness correction factor ($C = 0.005$). Emissivity values were assigned on the basis of the *NDVI* range. For $NDVI < 0$, the area was designated as water with an emissivity of 0.991. *NDVI* values between 0 and 0.2 indicated bare soil, with emissivity set at 0.996. *NDVI* ranging from 0.2 to 0.5 signified a mix of vegetation and bare soil, with emissivity calculated using Eq. (5). $NDVI > 0.5$ indicated fully vegetated areas with an emissivity of 0.973.

The *BT* was corrected for emissivity to calculate the *LST* using

$$LST = \frac{BT}{1 + \left( \lambda \times \frac{BT}{\rho} \right) \ln \varepsilon}, \tag{6}$$

where $\lambda$ represents the wavelength of Landsat 8 TIRS ($\lambda$ =10.895 μm) and $\rho$ denotes the second radiation constant of Planck's law ($\rho$ =1.438 × $10^{-2}$ m·K). The resultant *LST* values were recorded in degrees Celsius (°C) for further image segmentation and anomaly detection analysis.

To reduce systematic errors arising from temporal variations, the *RLST* was computed by standardizing *LST* values using

$$RLST_i = LST_i - LST_{mean}, \tag{7}$$

where $RLST_i$ represents the *RLST* for month $i$, $LST_i$ is the *LST* for month $i$, and $LST_{mean}$ denotes the average *LST* across all analyzed months.

### 2.5 Image segmentation and identification of high- and low-temperature core zones

In this study, an object-based multiresolution segmentation approach was employed to delineate spatial units for subsequent regression modeling. The segmentation was performed

using eCognition software, with the scale parameter set to 15 and the shape and compactness factors optimized to 0.5 and 0.1, respectively, to maintain the geometric integrity and clear boundaries of segmented objects. To mitigate discrepancies caused by temporal variations in imagery, a multitemporal fusion strategy was adopted, integrating the *LST* and *RLST* data from four selected time periods prior to segmentation.

On the basis of the segmentation results, average *LST* values were calculated for each spatial unit to preliminarily characterize the temperature distribution patterns within the city. To enhance the statistical robustness of spatial clustering, Getis-Ord Gi* hotspot analysis was conducted using ArcGIS Pro to detect statistically significant high-temperature (hotspot) and low-temperature (coldspot) clusters. By integrating the average *LST* values of the segmented units with the results of the hotspot analysis, potential high- and low-temperature core zones could be delineated for further investigation.

### 2.6 Selection of explanatory variables

To support the analysis of *LST* patterns, a set of explanatory variables was selected on the basis of literature review[18–20] and data availability. These variables were classified into three categories, namely, (1) land surface variables, (2) topographic variables, and (3) population and urban form variables, and were spatially assigned to the segmented units derived from the multiresolution image segmentation to ensure spatial consistency for subsequent regression modeling.

#### 2.6.1 Land surface variables

Land surface variables were derived from Korea's medium-classification land cover dataset and Landsat 8 imagery. The land cover dataset was used to calculate the proportion of surface types within each segmented unit and included water-related indicators such as water body density and distance to the nearest water body (Table 2). In addition, several spectral indices (Table 3) were derived from Landsat 8 imagery to quantify vegetation status, built-up intensity, and other surface conditions. All selected variables were incorporated as explanatory inputs for the regression analysis of *LST* variation.

#### 2.6.2 Topographic variables

Topographic variables were derived from the DEM, including elevation and slope. These variables were assigned to the segmented units and used as explanatory inputs in the regression analysis to evaluate their association with *LST* patterns (Table 4).

#### 2.6.3 Population and urban form variables

Population and urban form variables were selected to represent socio-spatial patterns influencing *LST*. This included population density, building footprint area, and road network

Table 2
Land surface variables.

| Category | Variable | Code | Description |
|---|---|---|---|
| Land Cover Type | Public Facilities Area | N1 | Environmental, educational, administrative, or public use areas |
| | Industrial Area | N2 | Areas for production, transportation, or mixed industrial use |
| | Orchard | N3 | Land for growing fruit trees |
| | Transportation Area | N4 | Airports, ports, roads, and other transport-related areas |
| | Other Cultivated Land | N5 | Areas for livestock, aquaculture, or ornamental crops |
| | Inland Water | N6 | Rivers, lakes, reservoirs, and dams |
| | Inland Wetland | N7 | Wetlands, estuaries, and riparian zones |
| | Paddy Field | N8 | Irrigated fields used for rice cultivation |
| | Cultural, Sports, and Recreational Facilities | N9 | Resorts, stadiums, exhibition sites, golf courses |
| | Upland Field | N10 | Dry farmland, including both managed and unmanaged fields |
| | Commercial Area | N11 | Retail, business, entertainment, and terminal zones |
| | Facility-based Cultivation Area | N12 | Areas with greenhouses, mushroom farms, nurseries |
| | Artificial Bare Land | N13 | Quarries, construction sites, and cleared areas |
| | Artificial Grassland | N14 | Man-made grasslands such as golf or ski courses |
| | Natural Bare Land | N15 | Naturally exposed terrain like tidal flats and rocky slopes |
| | Natural Grassland | N16 | Naturally formed grasslands near mountains or rivers |
| | Residential Area | N17 | Areas for residential, commercial, or public buildings |
| | Coniferous Forest | N18 | Forests with >75% coniferous tree cover |
| | Mixed Forest | N19 | Mixed forests with both coniferous and broadleaf trees (<75% each of the total area) |
| | Broadleaf Forest | N20 | Forests with >75% broadleaf tree cover |
| | Other Bare Land | N21 | Bare lands not classified elsewhere |
| Water-related Variables | Water Surface Area | Water_A | Water surface area within each spatial unit |
| | Water Body Density | Water_D | Density of water bodies per spatial unit |
| | Distance to the Nearest Water Body | Water_DT | Distance to the nearest water body (m) |

Table 3
Spectral indices.

| Variable | Code | Formula |
|---|---|---|
| Normalized Difference Vegetation Index | *NDVI* | $(NIR - RED)/(NIR + RED)$ |
| Normalized Difference Water Index | *NDWI* | $(NIR - SWIR)/(NIR + SWIR)$ |
| Normalized Difference Built-up Index | *NDBI* | $(SWIR - NIR)/(SWIR + NIR)$ |
| Soil Adjusted Vegetation Index | *SAVI* | $((NIR - RED)/(NIR + RED + L)) \times (1 + L)$, $L = 0.5$ |
| Enhanced Vegetation Index | *EVI* | $2.5 \times (NIR - RED)/(NIR + 6 \times RED - 7.5 \times BLUE + 1)$ |

Table 4
Topographic variables.

| Variable | Code | Description |
|---|---|---|
| Digital Elevation Model | DEM | Represents surface elevation |
| Slope | Slope | Rate of elevation change, derived from DEM |

density. All variables were spatially assigned to the segmented units and used as explanatory variables in the regression analysis (Table 5).

### 2.7 Data assignment and normalization

All variable values were calculated and assigned to the segmented spatial units using ArcGIS Pro 3.0. This process generated a region-level dataset for subsequent statistical analysis. To ensure comparability among variables and minimize the impact of scale differences in regression modeling, *Z*-score standardization was applied to *LST* and all explanatory variables using

$$Z = \frac{X - \mu}{\sigma}, \tag{8}$$

where $X$ represents the original variable value, $\mu$ is the mean, and $\sigma$ is the standard deviation. This standardization allows all variables to be analyzed within the same numerical range, enhancing the stability and interpretability of the regression model.

### 2.8 OLS and GWR analysis

#### 2.8.1 OLS model

OLS was used to examine the linear relationship between *LST* and the explanatory variables identified in Sect. 2.6. *LST* was set as the dependent variable, and the model was implemented using the OLS tool in ArcGIS Pro 3.0. The general expression is

$$Y_i = \beta_0 + \sum \beta_i X_i + \varepsilon_i, \tag{9}$$

where $Y_i$ represents the dependent variable, $X_i$ represents the independent variable, $\beta_0$ is the intercept, $\beta_i$ is the regression coefficient, and $\varepsilon_i$ is the random error term.

Table 5
Population and urban form variables.

| Category | Variable | Code | Description | Unit |
|---|---|---|---|---|
| Building | Building Area | Building_A | Total building area within each spatial unit | $m^2$ |
| | Building Density | Building_D | Proportion of building area within the unit | % |
| | Distance to Nearest Building | Building_DT | Distance to the nearest building | m |
| Road | Road Area | Road_A | Total road area within each spatial unit | $m^2$ |
| | Road Density | Road_D | Proportion of road area within the unit | % |
| | Distance to Nearest Road | Road_DT | Distance to the nearest road | m |
| Population | Population Density | Pop_D | Number of people per square kilometer | persons/$km^2$ |

As a global model, OLS assumes spatial stationarity, meaning that the relationships between variables are constant across space. To account for spatial heterogeneity, GWR was used to model spatially varying relationships between *LST* and its influencing variables.

### 2.8.2 GWR model

GWR was implemented in ArcGIS Pro 3.0 to account for spatial heterogeneity in *LST* and its explanatory variables. Unlike OLS, GWR is a local regression model that captures spatial non-stationarity by allowing model coefficients to vary across locations. The general form of the GWR model is expressed as

$$\mathcal{Y}_i\left(u_i, v_i\right) = B_o\left(u_i, v_i\right) + \sum_a^n B_a\left(u_i, v_i\right) x_{ia} + \delta_i\left(u_i, v_i\right), \tag{10}$$

where $\mathcal{Y}_i(u_i, v_i)$ represents the dependent variable at sample $i$, $B_o(u_i, v_i)$ is the intercept parameter for sample $i$, and $B_a(u_i, v_i)$ denotes the local regression coefficient of the $a$th spatial variable at sample $i$. $u_i$, $v_i$ represent the spatial coordinates of sample $i$, $n$ is the total number of independent variables, $x_{ia}$ is the independent variable at sample $i$, and $\delta_i(u_i, v_i)$ is the error term.

GWR incorporates a spatial weighting matrix to estimate location-specific coefficients, effectively revealing spatial variations in the relationships between *LST* and its influencing variables. In this study, the significant influencing variables identified through OLS were subsequently incorporated into the GWR model to explore how their effects vary across space. The bandwidth of the GWR model was selected automatically in ArcGIS Pro using the corrected Akaike Information Criterion (AICc), a method that balances model fit and complexity by minimizing residual variance while penalizing overfitting. This approach provides a deeper understanding of the spatial mechanisms underlying *LST* formation.

## 3. Results and Discussion

### 3.1 Spatiotemporal distribution of *LST* and *RLST*

To examine the seasonal variation in *LST* across Chuncheon, four representative dates were selected: March 15, June 19, October 25, and December 28. The spatial distribution of *LST* for each period is presented in Figs. 3(a)–3(d), with the corresponding statistical summaries shown in Table 6. The results reveal substantial seasonal differences, with the highest temperatures recorded in summer (12.47–37.80 °C) and the lowest in winter (−14.55–3.47 °C).

In spring, high-temperature zones were primarily observed in the city center, including commercial, residential, and transportation areas, and in agricultural areas in the southeast. These patterns likely result from active anthropogenic heat emissions, heat release from urban infrastructure, and increased surface heat absorption in exposed agricultural land owing to incomplete vegetation recovery. In summer, high *LST* values remained concentrated in the city center and were also evident in industrial zones, densely populated residential areas, and major

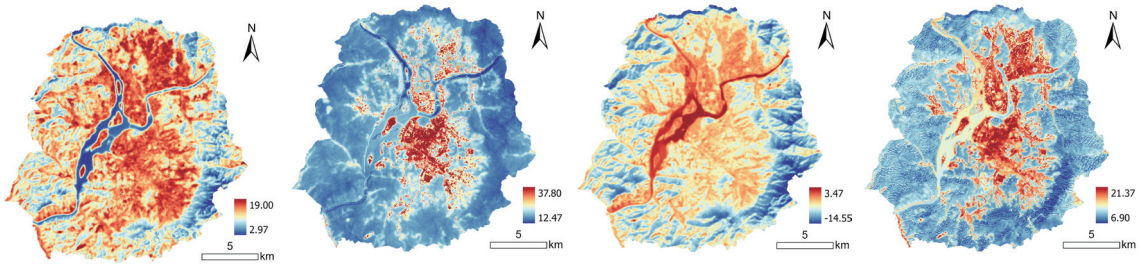


(a) (b) (c) (d)

Fig. 3. (Color online) Seasonal variation of *LST*: (a) March 15 (°C), (b) June 19 (°C), (c) October 25 (°C), and (d) December 28 (°C).

Table 6
Seasonal statistics of *LST*.

| Date | Mean (°C) | Max (°C) | Min (°C) | Std. Dev. (°C) |
|---|---|---|---|---|
| 3/15 | 10.98 | 19.00 | 2.97 | 2.62 |
| 6/19 | 22.01 | 37.8 | 12.47 | 3.53 |
| 10/25 | 12.02 | 21.37 | 6.90 | 2.44 |
| 12/28 | −5.09 | 3.47 | −14.55 | 2.83 |

Note: Max = Maximum; Min = Minimum; Std. Dev. = Standard Deviation

transportation corridors. These distributions were shaped by the combined effects of the UHI phenomenon, heat retention by impervious surfaces, low vegetation coverage, and increased human activity. In autumn, although the overall temperature decreased, high-temperature zones persisted in built-up and agricultural areas. Forested regions continued to maintain lower *LST*, primarily as a result of evapotranspiration and shading. In winter, relatively warm areas appeared near water bodies and certain farmlands, likely owing to water's thermal inertia and soil moisture retention. The lowest temperatures were consistently recorded in forested areas throughout the year, demonstrating their stable cooling function.

*RLST* exhibited spatial patterns closely aligned with those of the original *LST*, with only minor differences observed along the boundaries of high-temperature zones (Fig. 4). To reduce the impact of inter-seasonal temperature variation on the segmentation results, *RLST* was introduced as a normalized input in the multitemporal image segmentation process. This approach was aimed at improving the consistency of spatial unit delineation across different seasons.

### 3.2 Identification of core high-/low-temperature zones

Multiresolution segmentation was conducted using eCognition software to process *LST* and *RLST* images for four dates, resulting in a total of 340 spatial units. On the basis of these units, the Getis-Ord Gi* statistic was applied to the *LST* values for each season to detect significant spatial clusters of high and low temperatures. Figure 5 shows the seasonal *LST* distributions across the segmented units, while Fig. 6 presents the corresponding Gi* hotspot and coldspot patterns.

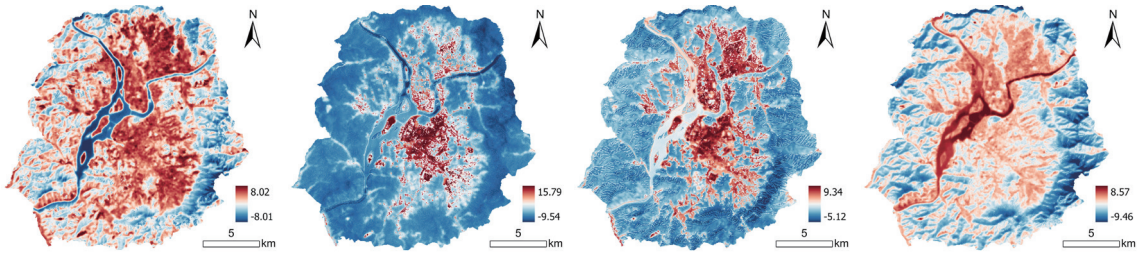


(a) (b) (c) (d)

Fig. 4. (Color online) Seasonal variation of *RLST*: (a) March 15 (°C), (b) June 19 (°C), (c) October 25 (°C), and (d) December 28 (°C).

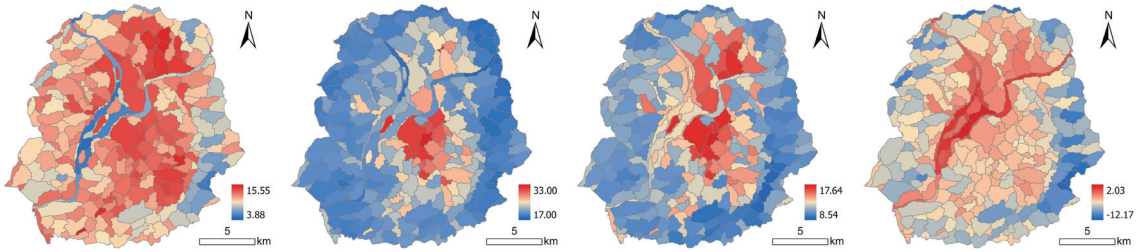


(a) (b) (c) (d)

Fig. 5. (Color online) Post-segmentation output incorporating *LST* results: (a) March 15 (°C), (b) June 19 (°C), (c) October 25 (°C), and (d) December 28 (°C).

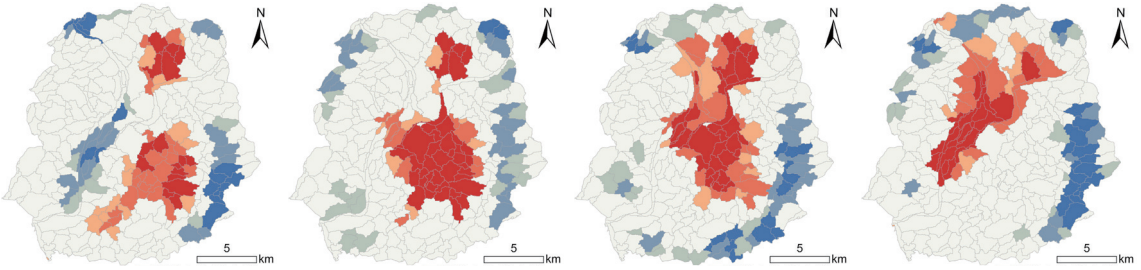


(a) (b) (c) (d)

Fig. 6. (Color online) Getis-Ord Gi* results: (a) March 15, (b) June 19, (c) October 25, and (d) December 28.

The results reveal that, in spring, summer, and autumn, hotspot clusters are primarily located in the city center and extended into surrounding urban–agricultural transition areas. In contrast, winter hotspots are mainly distributed near water bodies, which aligns closely with the seasonal distribution of high *LST* values. Coldspots are consistently found in forested areas across all seasons, indicating a stable cooling role of vegetated land cover in mitigating surface temperatures.

To further identify representative core zones, the top 20 highest and lowest *LST* units for each season were selected and compared with statistically significant hotspot and coldspot areas

identified through Gi* analysis. Spatial units that met both criteria, including extreme *LST* values and significant spatial clustering, were designated as high- and low-temperature core zones (Fig. 7).

### 3.3 Results of OLS and GWR model

To examine the driving factors influencing *LST* variations, we employed an OLS regression model based on 340 spatial units generated through multiresolution segmentation. The OLS regression model was used for an initial assessment of the relationships between *LST* and a set of explanatory variables. To control multicollinearity, only variables with a variance inflation factor (VIF) less than 7.5 were included. GWR was then applied to further explore the spatial heterogeneity of significant predictors.

The OLS results for each season (Table 7) show strong explanatory power, with $R^2$ values of 0.95 (spring), 0.95 (summer), 0.94 (autumn), and 0.96 (winter), as well as corresponding adjusted $R^2$ values of 0.94, 0.95, 0.93, and 0.96. *F*-tests for all seasons were significant at the 99% confidence level ($p < 0.01$), confirming the robustness of the models.

Table 8 shows the key variables significantly associated with *LST* across seasons. Land cover variables such as N1, N8, and N12 were significant in multiple seasons. N1 and N12 showed consistent positive correlations with *LST* in spring, autumn, and winter. In contrast, N8 was negatively associated in these seasons. N15 and N19 exhibited seasonal shifts in their relationships with *LST*. Among topographic variables, DEM showed a consistent negative correlation with *LST* across all seasons, indicating a stable cooling effect of higher altitudes. Regarding urban morphological factors, Water_A showed a cooling effect in summer and autumn, with the strongest association observed in autumn. Building_D was positively associated with *LST* in autumn, while Road_D showed a similar effect in winter. The influence

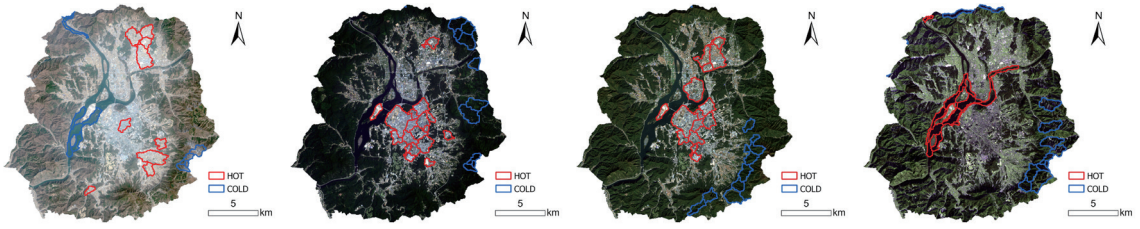


(a) (b) (c) (d)

Fig. 7. (Color online) High-/low-temperature core zones: (a) March 15, (b) June 19, (c) October 25, and (d) December 28.

Table 7
OLS results for each season.

| Date | 3/15 | 6/19 | 10/25 | 12/28 | (mean) |
|---|---|---|---|---|---|
| $R^2$ | 0.95 | 0.95 | 0.94 | 0.96 | 0.95 |
| Adjusted $R^2$ | 0.94 | 0.95 | 0.93 | 0.96 | 0.95 |
| AICc | 67.77 | 17.47 | 109.01 | −52.61 | 35.41 |

Table 8
Significant explanatory variables for *LST* across seasons (OLS results).

| Variable | 3/15 | 6/19 | 10/25 | 12/28 |
|---|---|---|---|---|
| N1 | 0.052 | – | 0.0363 | 0.0348 |
| N2 | – | – | 0.0268 | – |
| N3 | – | – | −0.0391 | – |
| N7 | −0.0698 | – | −0.0371 | – |
| N8 | −0.0743 | – | −0.0779 | −0.0481 |
| N12 | 0.0158 | – | 0.0266 | 0.0163 |
| N13 | – | −0.0703 | – | – |
| N15 | – | – | −0.0305 | 0.029 |
| N18 | – | 0.0541 | – | −0.0475 |
| N20 | – | – | – | 0.047 |
| N21 | – | – | – | 0.0289 |
| DEM | −0.4563 | −0.0876 | −0.2079 | −0.4269 |
| Water_A | 0.0751 | −0.1509 | −0.0935 | 0.0596 |
| Road_D | – | – | – | 0.0985 |
| Road_DT | – | −0.0575 | – | 0.0528 |
| Building_D | – | - | 0.2059 | – |

of Road_DT varied between summer and winter, suggesting potential interactions with seasonal urban heat dynamics.

Overall, the results of the analysis indicate that the driving factors of *LST* varied significantly across seasons. While the influence of land cover remained relatively stable, topographic and urban morphological variables exhibited more pronounced seasonal variability. These results highlight the complex and seasonally dynamic nature of *LST* regulation.

Table 9 presents the GWR estimation results for the variables selected from the OLS model. In addition, the residuals derived from the GWR model were examined to assess their spatial randomness. The results indicated that the residuals were randomly distributed in space, with no significant clustering observed (Fig. 8). Figures 9–12 illustrate the spatial distributions of coefficients across four seasons. In these figures, positive and negative values represent positive and negative correlations with *LST*, respectively, while stronger color saturation indicates greater impact intensity.

With respect to topographic factors, DEM exhibited a consistently negative correlation with *LST* across all seasons, suggesting that higher elevations are generally associated with lower surface temperatures. In contrast, Water_A showed a negative association in most regions, though some localized areas, particularly in winter, a positive relationship was observed. This implies potential regional differences in the seasonal regulation effects of water bodies.

For urban morphological factors, Road_DT had a negative impact on *LST* in June, while in December, both Road_DT and Road_D showed considerable spatial variability in effect direction and magnitude. The effect of Building_D in October was spatially mixed, with both positive and negative associations observed across regions.

Regarding land cover variables, N1 was positively associated with *LST* in spring and autumn but showed a spatially varied pattern in winter. N8 generally exhibited a positive correlation in spring, autumn, and winter, although some areas displayed localized negative effects. N2 and N21 were positively correlated with *LST* in autumn and winter, respectively, while N3 had a

Table 9
GWR results for each season.

| Date | 3/15 | 6/19 | 10/25 | 12/28 | (mean) |
|---|---|---|---|---|---|
| $R^2$ | 0.64 | 0.74 | 0.70 | 0.75 | 0.71 |
| Adjusted $R^2$ | 0.60 | 0.70 | 0.65 | 0.72 | 0.67 |
| AICc | 674.84 | 580.06 | 651.20 | 552.10 | 614.55 |
| Sigma | 0.63 | 0.55 | 0.59 | 0.53 | 0.57 |

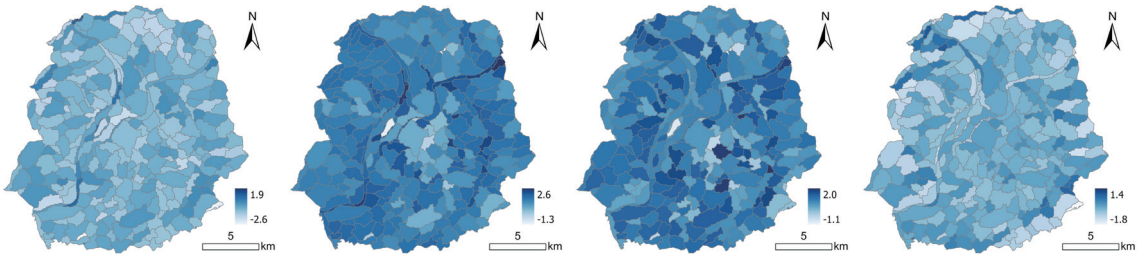


(a) (b) (c) (d)

Fig. 8. (Color online) Spatial distribution of residuals from the GWR model: (a) March 15, (b) June 19, (c) October 19, and (d) December 28.

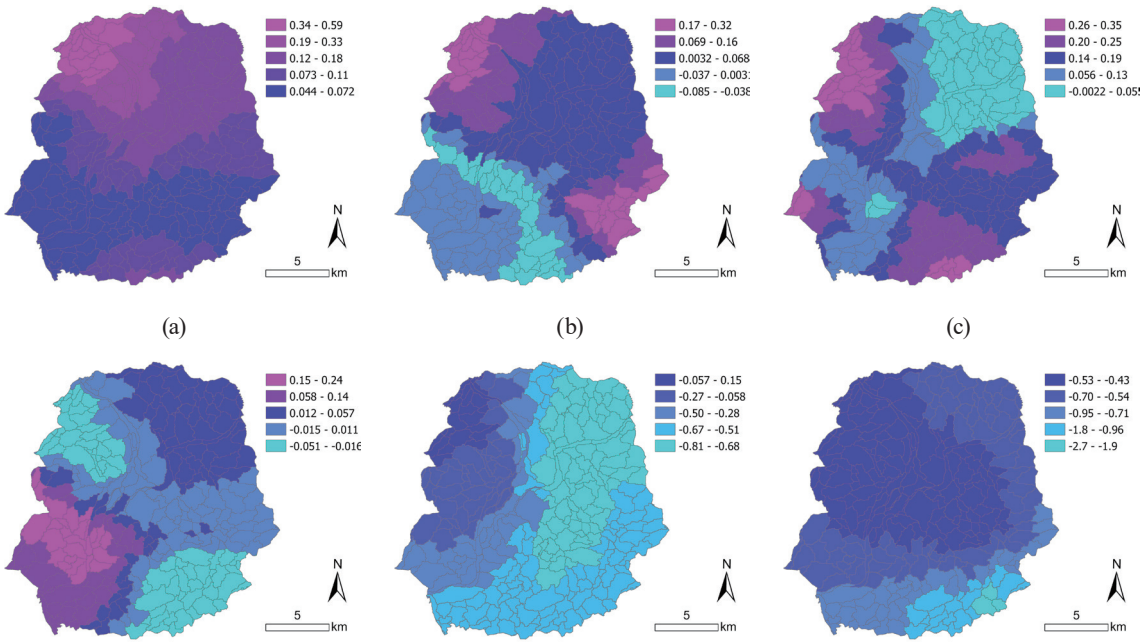


(a) (b) (c)

(d) (e) (f)

Fig. 9. (Color online) GWR coefficient distribution on March 15: (a) N1, (b) N7, (c) N8, (d) N12, (e) DEM, and (f) Water_A.

consistent negative effect only in autumn. Variables such as N7, N12, N13, N15, and N20 displayed considerable spatial variation depending on the season and region. In contrast, N18 showed a consistently negative effect on *LST* in both summer and winter.

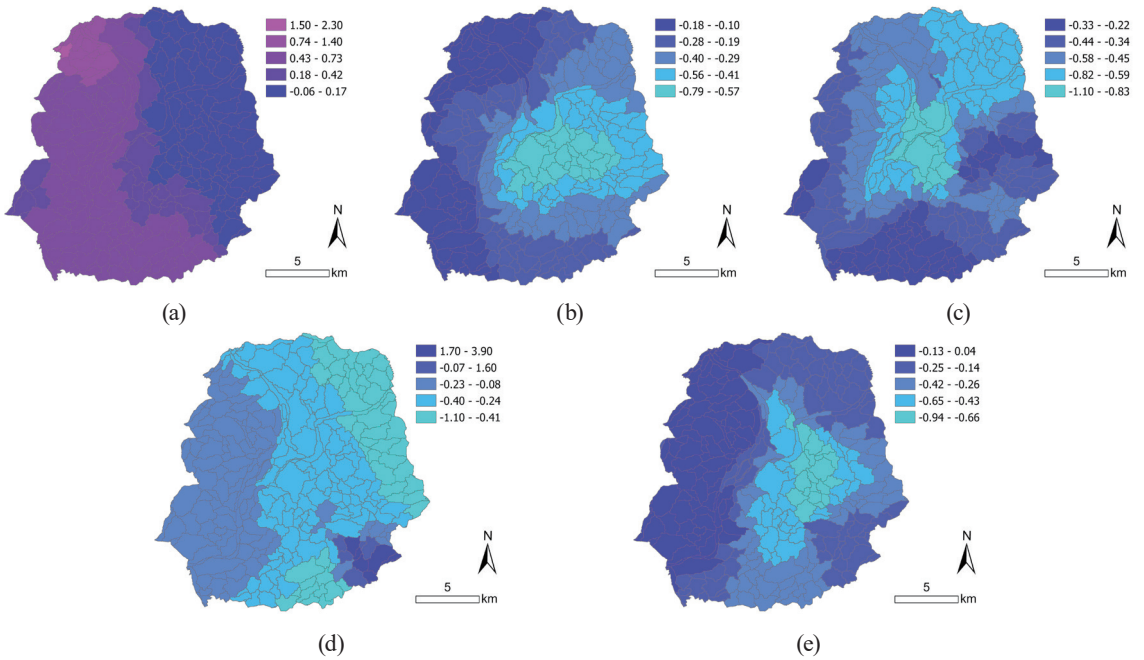


Fig. 10. (Color online) GWR coefficient distribution on June 19: (a) N13, (b) N18, (c) DEM, (d) Water_A, and (e) Road_DT.

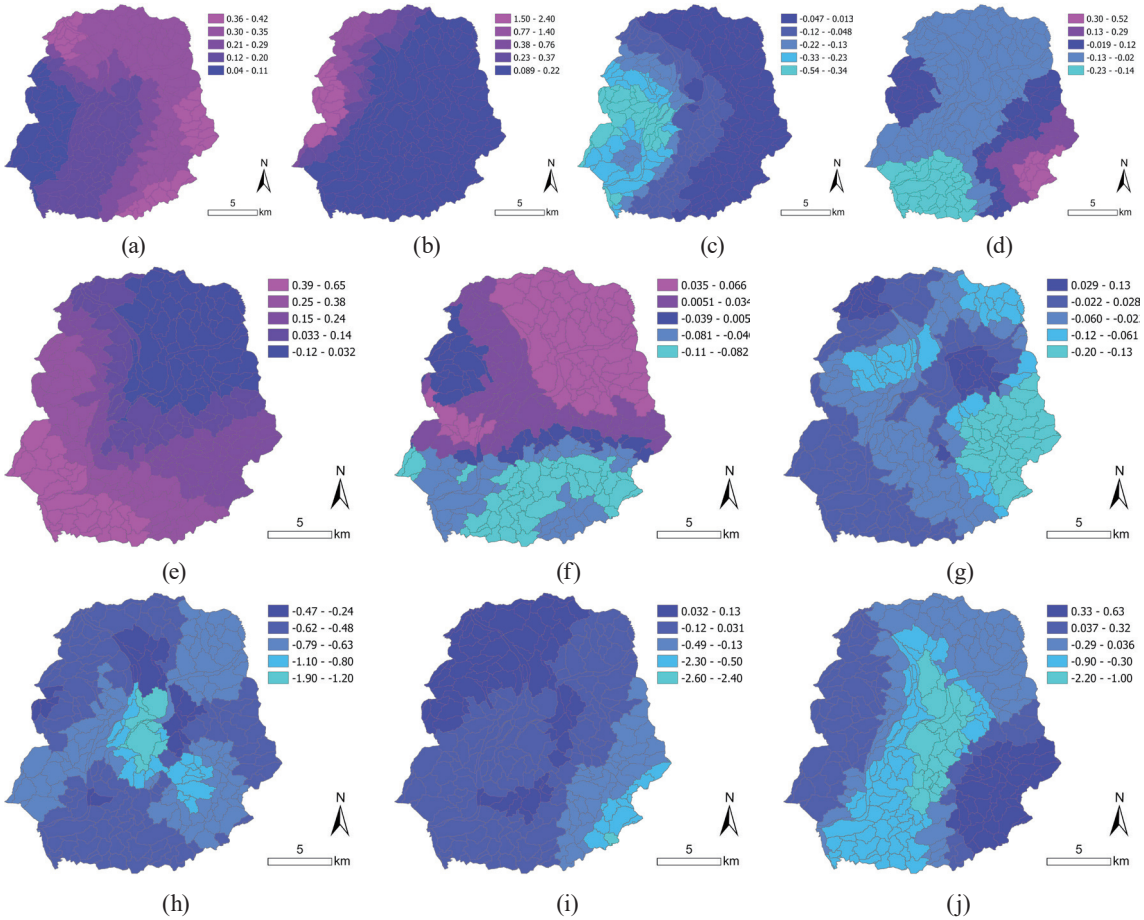


Fig. 11. (Color online) GWR coefficient distribution on October 25: (a) N1, (b) N2, (c) N3, (d) N7, (e) N8, (f) N12, (g) N15, (h) DEM, (i) Water_A, and (j) Building_D.

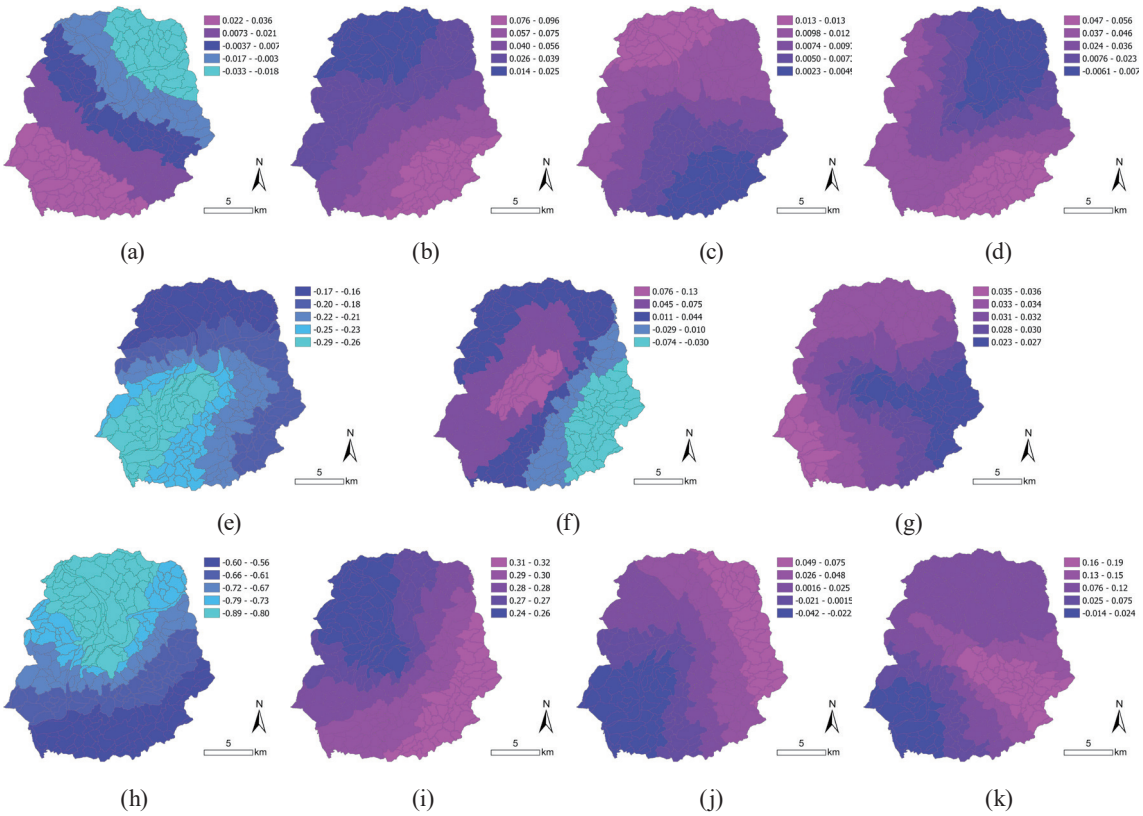


Fig. 12. (Color online) GWR coefficient distribution on December 28: (a) N1, (b) N8, (c) N12, (d) N15, (e) N18, (f) N20, (g) N21, (h) DEM, (i) Water_A, (j) Road_D, and (k) Road_DT.

Overall, the GWR results revealed substantial spatial heterogeneity in the effects of environmental variables on *LST*. The direction and strength of influence varied not only across seasons, but also among regions, emphasizing the importance of spatial context in understanding *LST* regulation.

To further examine variable behavior under extreme conditions, the spatial characteristics of significant factors were analyzed within core high- and low-temperature zones. While most variables exhibited trends consistent with citywide patterns, their spatial intensity and sensitivity were more pronounced in extreme areas. For example, N18 exerted a stronger cooling effect in low-temperature core zones during summer and winter, suggesting a stabilizing role under thermal extremes. Water_A, though generally cooling in spring and summer, showed positive correlations in high-temperature core zones in autumn and winter—possibly owing to the seasonal thermal retention capacity of water bodies. DEM remained negatively associated with *LST* across all seasons, with even stronger effects in core zones, reinforcing the importance of elevation under extreme conditions.

Urban morphological factors also exhibited heightened sensitivity in core zones. BUILD_D was positively associated with *LST* in autumn hotspots. ROAD_D showed contrasting effects in winter: it contributed to warming in cold zones but had a cooling influence in hot zones. ROAD_DT also displayed distinct seasonal and spatial shifts, reflecting the complex interactions between urban form and surface temperature.

In summary, while the spatial patterns of *LST* determinants in core zones generally aligned with citywide trends, the intensity and direction of several variables—particularly DEM, Water_A, and urban morphological indicators—were more spatially heterogeneous. These findings underscore the spatially non-stationary and multifactorial nature of *LST* regulation, especially in thermally extreme urban environments.

## 4. Conclusions

In this study, we examined the spatiotemporal patterns of *LST* in Chuncheon, South Korea, and identified the key driving factors using multiresolution segmentation, OLS, and GWR models. The results revealed distinct seasonal variations in *LST* distribution, with high temperatures predominantly concentrated in built-up and low-lying areas during summer, while forested and elevated regions consistently exhibited lower surface temperatures across all seasons. *LST* was significantly affected by land surface, topography, urban morphological, and population factors, with notable temporal and spatial variability.

Forests and DEM consistently produced cooling effects in both summer and winter, underscoring their importance in thermal regulation. Since DEM is static, it serves better as a contextual factor than as a planning variable. In contrast, urban morphological features showed strong spatial and seasonal heterogeneity, particularly in temperature hotspots and coldspots. Such detailed spatial differentiation is made possible through high-resolution satellite sensing, which captures surface thermal variability across diverse urban landscapes.

From a planning perspective, the results call for spatially differentiated heat mitigation strategies. In high-temperature zones, measures such as expanding green infrastructure, optimizing water bodies, and managing urban density can reduce thermal risks. Cooler areas provide insights for design adaptation. Overall, the findings offer a scientific basis for climate-adaptive zoning and heat-resilient urban design, emphasizing that one-size-fits-all solutions are inadequate. The integration of satellite-based *LST* monitoring into urban planning enables the continuous sensing and evaluation of thermal environments, facilitating data-driven heat mitigation strategies. Integrating sensor-based *LST* monitoring into urban planning can support the continuous observation and evaluation of the urban thermal environment, facilitating data-driven heat-mitigation strategies.

Despite these contributions, several limitations should be acknowledged. In the analysis, four daytime *LST* observations were used, which may not fully represent temporal variability. Nighttime thermal behavior and anthropogenic heat emissions were not considered. In addition, static land cover and morphological variables may underestimate land-use change effects. Moreover, the diagnosis of multicollinearity among explanatory variables relied solely on VIF, which provides a limited assessment. Future work will incorporate more comprehensive diagnostic methods. Future research should leverage multisource satellite sensors and higher-temporal-resolution data to improve *LST* retrieval accuracy and enhance the understanding of surface thermal dynamics.

## Acknowledgments

This study was supported by the Technology Development Project for Creation and Management of Ecosystem based Carbon Sinks (RS-2023-00218245) through KEITI, Ministry of Environment, and by a research grant of Kangwon National University in 2023.

## References

1 R. Cichowicz and A.D. Bochenek: Anthropocene. **46** (2024) 100433. https://doi.org/10.1016/j.ancene.2024.100433
2 L. Liu and Y. Zhang: Remote Sens. **3** (2011) 1535. https://doi.org/10.3390/rs3071535.
3 Z. Shi, X. Li, T. Hu, B. Yuan, P. Yin, and D. Jiang: Urban Clim. **49** (2023) 101529. https://doi.org/10.1016/j.uclim.2023.101529
4 H. Du, W. Cai, Y. Xu, Z. Wang, Y. Wang, and Y. Cai: Urban For. Urban Green. **27** (2017) 24. https://doi.org/10.1016/j.ufug.2017.06.008
5 H. S. Lopes, D. G. Vidal, N. Cherif, L. Silva, and P. C. Remoaldo: J. Environ. Manage. **376** (2025) 124446. https://doi.org/10.1016/j.jenvman.2025.124446
6 D. Zhou, L. Zhang, L. Hao, G. Sun, Y. Liu, and C. Zhu: Sci. Total Environ. **544** (2016) 617. https://doi.org/10.1016/j.scitotenv.2015.11.168
7 M. K. Firozjaei, S. Fathololoumi, M. Kiavarz, J. J. Arsanjani, and S. K. Alavipanah: Ecol. Indic. **109** (2020) 105816. https://doi.org/10.1016/j.ecolind.2019.105816
8 A. Kazemi, G. T. Cirella, A. Hedayatiaghmashhadi, and M. Gili: IEEE J. Sel. Top. Appl. Earth Observ. Remote Sens. **18** (2025) 7100. https://doi.org/10.1109/JSTARS.2025.3541406
9 J. He, W. Zhao, A. Li, F. Wen, and D. Yu: Int. J. Remote Sens. **40** (2019) 1808. https://doi.org/10.1080/01431161.2018.1466082
10 H. Su, G. Han, L. Li, and H. Qin: Sust. Cities Soc. **74** (2021) 103217. https://doi.org/10.1016/j.scs.2021.103217
11 E. A. Njoku and D. E. Tenenbaum: Remote Sens. Appl.-Soc. Environ. **27** (2022) 100780. https://doi.org/10.1016/j.rsase.2022.100780
12 A. Kashki, M. Karami, R. Zandi, and Z. Roki: Urban CLim. **37** (2021) 100832. https://doi.org/10.1016/j.uclim.2021.100832
13 T. Chakraborty and X. Lee: Int. J. Appl. Earth Obs. Geoinf. **74** (2019) 269. https://doi.org/10.1016/j.jag.2018.09.015
14 L. Yang, K. Yu, J. Ai, Y. Liu, W. Yang, and J. Liu: Remote Sens. **14** (2022) 1266. https://doi.org/10.3390/rs14051266
15 S. Ning, Y. Zhou, M. Wang, B. Li, P. Li, L. Zhang, and Y. Luo: Sustainability. **16** (2024) 9103. https://doi.org/10.3390/su16209103
16 U. Avdan and G. Jovanovska: J. Sens. **2016** (2016) 1. https://doi.org/10.1155/2016/1480307
17 J.A. Sobrino, J.C. Jiménez-Muñoz, and L. Paolini: Remote Sens. Environ. **90** (2004) 434. https://doi.org/10.1016/j.rse.2004.02.003
18 A. Guo, J. Yang, X. Xiao, J. Xia (Cecilia), C. Jin, and X. Li: Sust. Cities Soc. **53** (2020) 101972. https://doi.org/10.1016/j.scs.2019.101972
19 X. Li and W. Zhou: Sust. Cities Soc. **48** (2019) 101518. https://doi.org/10.1016/j.scs.2019.101518
20 W. Liu, Q. Meng, M. Allam, L. Zhang, D. Hu, and M. Menenti: Remote Sens. **13** (2021) 2858. https://doi.org/10.3390/rs13152858

## About the Authors

Zhien Li is a Ph.D. student of landscape architecture at Kangwon National University. She received her B.S. degree in landscape architecture from Beihua University in 2018 and her M.S. degree in the same field from Kangwon National University in 2024. Her research interests include remote sensing, land cover classification, and urban climate analysis.
(lizhien@kangwon.ac.kr)

Sung-Ho Kil is an associate professor at Kangwon National University. He graduated from Kangwon National University in 2003, majoring in landscape architecture. He earned his MLA and Ph.D. degrees from Seoul National University in 2007 and 2014, respectively. His research interests include ecological restoration, spatial ecology, and landscape ecology.
(sunghokil@kangwon.ac.kr)

Eunseok Lee received his B.S in environmental and urban engineering from Yonsei University (2001) and his M.S. and Ph.D. degrees in landscape architecture from the Graduate School of Environmental Studies at Seoul National University in 2007 and 2015, respectively. From 2018 to now, he has been the head of the National Green Building Center at AURI, South Korea. Since 2015, he has been a research fellow at Architecture and Urban Research Institute under the Office of the Prime Minister, South Korea. His research focuses on urban climate and GIS-based vulnerability assessment.
(enlee@auri.re.kr)

Sang-Jin Lee is a research professor at the Agricultural Science Research Institute of Chungnam National University. He received his B.S. in forest environmental resources in 2004 and subsequently earned his master's and Ph.D. degrees from Chungnam National University in 2008 and 2015, respectively. His research interests include forest soils, carbon storage in forest ecosystems, and environmental restoration.
(sangjin78@gmail.com)

Sungmin Lee is an assistant professor in the Department of Landscape Architecture and Urban Planning at Texas A&M University. He earned his bachelor's and master's degrees in landscape architecture from Seoul National University in 2007 and 2009, respectively. He earned his Ph.D. degree in 2018 from Texas A&M University. His primary research interests are in addressing the needs of vulnerable populations such as older adults, the benefits of green space, and the mitigation of health disparities and environmental inequalities.
(sungminlee@tamu.edu)